ARTICLES SCIENCE CHINA Materials

mater.scichina.com link.springer.com

Published online 7 December 2018 | https://doi.org/10.1007/s40843-018-9377-3

Sci China Mater 2019, 62(6): 790–796

Organic-inorganic hybrid Sn-based perovskite photodetectors with high external quantum efficiencies and wide spectral responses from 300 to 1000 nm

Yukun Wang[1,2], Dezhi Yang[1], Dongge Ma[1,3*], Dong Ha Kim[2], Tansir Ahamad[3], Saad M. Alshehri[3] and Agafonv Vadim[4]

ABSTRACT **Organic-inorganic hybrid perovskites are ideal materials for photodetection owing to their high charge carrier mobility, long charge carrier diffusion length, low dark current density and sharp absorption edge. However, a relatively small band gap (1.6 eV) limits their photon-harvesting efficiency in the near-infrared region. In the present work, we demonstrate a hybrid methylamine iodide and Pb-Sn binary perovskite as the light absorption layer in photodetectors. Experimentally, the wavelength of photo-response onset for the photodetectors can be extended to as great as 1,000 nm when the Sn content of the hybrid perovskite is increased to 30 mol%. In addition, the photodetectors exhibit a photoresponsivity of 0.39 A W^{-1}, a specific detectivity of 7×10^{12} Jones, a fast photoresponse with rise and decay time constants and an external quantum efficiency greater than 50% in the wavelength range of 350–900 nm, with a maximum value of about 80% at 550 nm.**

Keywords: organic-inorganic hybrid perovskite, photodetector, external quantum efficiency, spectral response, specific detectivity

INTRODUCTION

Organic-inorganic hybrid perovskites have been considered to be one of the most promising materials for solar energy harvesting and other optoelectronic devices due to long excitation diffusion length, high charge carrier mobility, direct band gap and large absorption coefficient [1–5]. In fact, the power conversion efficiency (PCE) of these materials has increased over the past nine years from 3.8% to the current record of 22.1% [6–14]. In addition to organic-inorganic hybrid perovskites, some all-inorganic perovskites also attracted the attention of researchers [15,16].

A broad community of researchers also paid attention to perovskite photodetectors [17]. Yang *et al.* [18] were the first to demonstrate an organic-inorganic hybrid perovskite photodetectors with an inverted device configuration in 2014. Interestingly, the inverted conjugated polymer (poly [(9,9-bis(3'-(*N*,*N*-dimethylamino) propyl)-2,7-fluorene)-alt-2,7-(9,9–dioctylfluorene)], PFN) provided an additional electric field that prevented hole injection and suppressed the dark current density. The resulting specific detectivity (D^*) approached 10^{14} Jones. Huang *et al.* [19] also reported a device interface engineering, where, after replacing the conductive polymer composed of poly(3,4-ethylenedioxythiophene) (PEDOT) doped with poly(styrenesulfonate) (PSS), denoted as PEDOT:PSS, with *N*4,*N*4'-bis(4-(6-((3-ethyl-oxetan-3-yl)methoxy)hexyl)phenyl)-*N*4,*N*4'-diphenylbi-phenyl-4,4'-diamine (OTPD), the highly sensitive photo-detector device demonstrated a high average external quantum efficiency (EQE) approaching 90%, a large linear dynamic range (LDR) of 94 dB, and a short response time of 120 ns. Analogously, Paul *et al.* [20] optimized the thickness of the transport layer in the

[1] Institute of Polymer Optoelectronic Materials and Devices, State Key Laboratory of Luminescent Materials and Devices, South China University of Technology, Guangzhou 510640, China
[2] Department of Chemistry and Nano Science, Ewha Womans University, 52, Ewhayeodae-gil, Seodaemun-gu, Seoul 03760, Korea
[3] Department of Chemistry, College of Science, King Saud University, Riyadh 11451, Kingdom of Saudi Arabia
[4] Moscow Institute of Physics and Technology Dolgoprudny, Moscow Region 141700, Russia
* Corresponding author (email: msdgma@scut.edu.cn)

photodetector based on an organic-inorganic hybrid perovskite light absorption layer to achieve low noise, infrared (IR)-blind visibility and high D^*. For all the above discussed photodetectors, the light absorption layer was composed of $CH_3NH_3PbI_3$ (or $CH_3NH_3PbI_{3-x}Cl_x$). However, due to the small band gap (1.6 eV) [21,22], these devices provided a photoresponse onset at about 800 nm, which hindered the efficient harvesting of photons in the near-IR (NIR) region. Therefore, the key to further enhance the performance of organic-inorganic hybrid perovskite photodetectors is to broaden the photoresponse into the NIR region. Although a photoresponse up to 950 nm was reported using polymer-perovskite hybrid thin films as the light absorber in our recent work [23], these photodetectors yielded only an EQE of ~60% in the visible region of the spectrum, which is less than most organic-inorganic hybrid perovskite photodetectors. Recently, Fan *et al.* [24] reported lead-free perovskite photodetectors with drastically improved stability, but they showed a detectivity lower than 10^{11} Jones.

The present study aims to resolve this deficiency in our previous work by a hybrid CH_3NH_3I and Pb-Sn binary perovskite with a layered structure composed of indium tin oxide (ITO), PEDOT:PSS, $CH_3NH_3Pb_{1-x}Sn_xI_3$, C_{60} and Al layers, which serves as the front contact, hole extraction, light absorption layer, electron extraction and back contact, respectively. The hybrid perovskite thin films were formed by the deposition of a mixture of tin iodide (SnI_2) with a molar content defined by x and lead iodide (PbI_2) with a molar content defined by $1-x$, followed by the deposition of CH_3NH_3I [25]. The hybrid perovskite photodetector with a Sn content of 30 mol% (i.e., x=0.3) provided the best photon harvesting performance with a NIR photoresponse of 1,000 nm.

EXPERIMENTAL SECTION

CH_3NH_3I was synthesized *via* the reaction of 24 mL methylamine (33 wt.% in ethanol; Aldrich) and 10 mL hydroiodic acid (57 wt.% in water; Aladdin) in 100 mL ethanol in an ice bath for 2 h with stirring [26]. The precipitate was collected using a rotary evaporator at 50°C to remove the solvent, and the product was recrystallized from ethanol. The crystals were filtered and washed three times with diethyl ether, and the solid was dried at 60°C in a vacuum oven overnight. All other materials were purchased from commercial sources.

All photodetectors were fabricated on commercial ITO patterned glass electrode substrates. As illustrated in Fig. 1, PEDOT:PSS (Clevios™ P VP Al 4083, Heraeus) was spin-coated on the ITO at 5,000 rpm for 55 s and cured in a furnace at 120°C for 20 min in air. $CH_3NH_3Pb_{1-x}Sn_xI_3$ layers in our photodetector devices were prepared by the interdiffusion of PbI_2 and SnI_2 induced by thermal annealing [24]. Briefly, a mixture of PbI_2 and SnI_2 was deposited by spin coating on the PEDOT:PSS surface using a ($[PbI_2]_{1-x}$+$[SnI_2]_x$) and *N*,*N*-dimethylformamide (DMF) solution. The perovskite composition depended on x of 0, 0.15, 0.3, 0.5 and 1.0. A CH_3NH_3I layer was spin-coated on the top of the PbI_2 and SnI_2 film, followed by annealing at 110°C for 45 min [25]. Then, a 50 nm C_{60} layer was evaporated on the $CH_3NH_3Pb_{1-x}Sn_xI_3$ layer surface at a rate of 0.05 nm s^{-1}. Finally, a 100 nm Al layer was deposited by thermal evaporation on the C_{60} surface. The area of these devices is 0.08 cm^2.

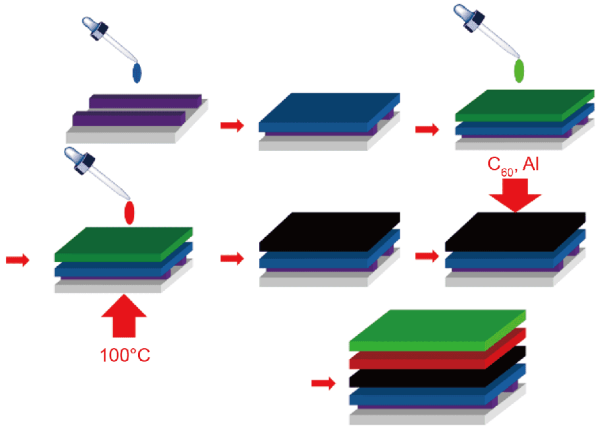

Figure 1 Schematic diagram illustrating the fabrication steps and architecture of the resulting hybrid perovskite photodetectors. PEDOT:PSS (blue) was spin-coated on the ITO side (purple) of the substrates. A mixture of PbI_2 and SnI_2 (green) was deposited by spin coating on the PEDOT:PSS surface using a ($[PbI_2]_{1-x}$+$[SnI_2]_x$) and DMF solution. A second layer consisting of CH_3NH_3I (red) was spin-coated on the top of the PbI_2 and SnI_2 film, followed by annealing. $CH_3NH_3Pb_{1-x}Sn_xI_3$ layer was painted black. Then, C_{60} and Al layer were deposited by thermal evaporation. More details were shown in experimental process.

RESULTS AND DISCUSSION

Fig. 2a shows the crystal structure of the hybrid $CH_3NH_3Pb_{1-x}Sn_xI_3$ perovskite, where the red spheres (A), blue spheres (X) and green spheres (B) are CH_3NH_3 groups, I and Pb or Sn, respectively. Theoretically, the stability of this hybrid perovskite structure can be evaluated according to a tolerance factor α, defined as follows [27]: $\alpha=(r_A+r_X)/(2^{1/2}(r_B+r_X))$ (1), where r_A, r_B and r_X are the atomic radii of A, B and X, respectively. For a stable hybrid perovskite structure, α should be between 0.813 and 1.107 [28]. We can calculate α for a hybrid Pb-Sn binary perovskite according to standard atomic radii,

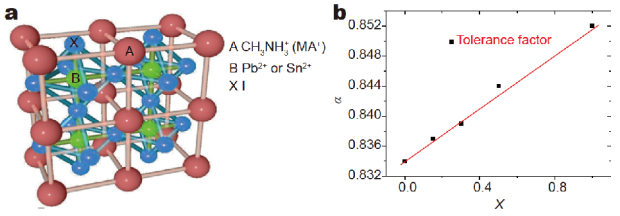

Figure 2 (a) Theoretical crystal structure of the hybrid perovskite, where the red spheres: CH_3NH_3 groups (A), blue spheres (X): I, and green spheres (B): Pb or Sn. (b) Tolerance factor (α) of the hybrid Pb-Sn binary perovskite plotted according to Equation (1) as a function of molar Sn content (x).

and plot the results according to x (Fig. 2b). The α for $CH_3NH_3PbI_3$ (i.e., x=0) is 0.834 and that for $CH_3NH_3SnI_3$ (i.e., x=1) is 0.852. Therefore, the hybrid Pb-Sn binary perovskite is stable for all x. This theoretical finding is further verified experimentally by the following results.

X-ray diffraction (XRD) patterns of $CH_3NH_3PbI_3$, $CH_3NH_3Pb_{0.85}Sn_{0.15}I_3$, $CH_3NH_3Pb_{0.7}Sn_{0.3}I_3$, $CH_3NH_3Pb_{0.5}Sn_{0.5}I_3$ and $CH_3NH_3SnI_3$ hybrid perovskite films deposited on PEDOT:PSS are presented in Fig. 3a. The primary XRD peaks obtained for all of these hybrid perovskites are found at about 14° and 28°, which are ascribed to (110) and (220) lattice planes, respectively, and lead to a tetragonal crystal structure [29]. In the optical absorption spectra (Fig. 3b), the electronic absorption edges of these perovskite thin films present an obvious shift to higher wavelengths (i.e., a red-shift) with increasing x. We also note that the optical absorption of the $CH_3NH_3PbI_3$ film decreases rapidly around 780 nm, while the absorption edges of all other films decrease gradually in a long-tailed fashion. After Sn was added into Pb-based perovskite, the bandgap of perovskite will be shortened. Hence, perovskite thin films demonstrated narrowing optical absorption bands with the increase of Sn (Fig. 3c). These results indicate that Sn is helpful for broadening the hybrid perovskite photoresponse.

In Fig. 4, the surface morphologies of $CH_3NH_3PbI_3$, $CH_3NH_3Pb_{0.85}Sn_{0.15}I_3$, and $CH_3NH_3Pb_{0.7}Sn_{0.3}I_3$ are very similar, while $CH_3NH_3Pb_{0.5}Sn_{0.5}I_3$ and $CH_3NH_3SnI_3$ exhibit obvious pinholes. As found in many reports, it may be due to the rapid crystallization of Sn-based perovskite making it difficult to fabricate compact and uniform perovskite films [30].

The device structure used in this study is shown in Fig. 5a. Fig. 5b presents typical EQE spectra under a short circuit condition for all hybrid perovskite photodetectors. In the case of x=0, the EQE exhibits a high peak value (~85%) in the visible light region and a photoresponse onset at ~800 nm due to its band gap of 1.6 eV, leading to a wide spectral range in the NIR region that remains unused and thus hindering the efficient photon harvesting of the photodetector. However, with increasing x from 0 to 0.3, the EQE decreases only slightly below 800 nm, while the spectra exhibit obvious red-shifts to wavelengths greater than 800 nm. Here, the photoresponse onset with x=0.15 is ~900 nm, while that with x=0.3 is ~1,000 nm. However, with x=0.5, although the photoresponse onset exceeds 1,000 nm, the EQE in the visible light region is strongly attenuated compared with devices with lower Sn content. Moreover, the photodetector employing the $CH_3NH_3SnI_3$ hybrid perovskite thin film with all Pb replaced by Sn exhibits no photoresponse [31]. This indicates that the Sn content affects the wavelength range of the photoresponse of the hybrid perovskite photodetectors, and implies that, if the Sn content is not too high, the photoresponse can be broadened. In addition, we measured the monochromatic NIR photoresponse of the two photodetector devices with x=0.15 and 0.3 as a function of bias voltage (Fig. 5c). Here, we note that, at 900 nm, the EQE of the photodetector with x=0.3 is about 50% greater than that with x=0.15. If the optical wavelength is shifted to

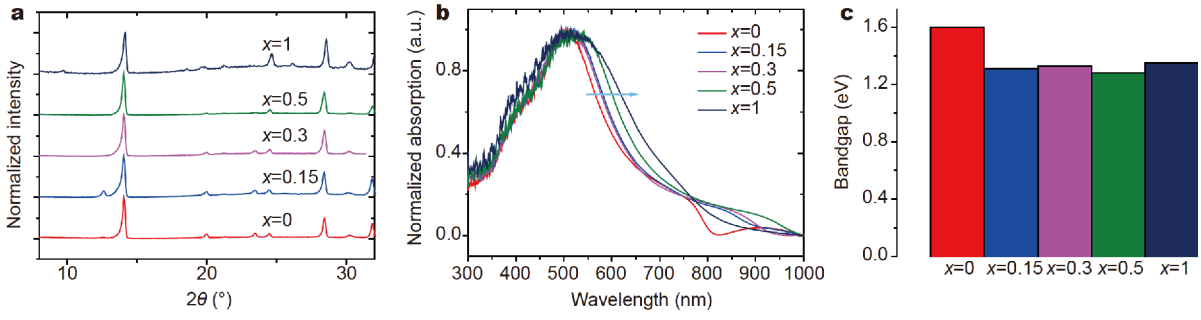

Figure 3 (a) XRD patterns, (b) optical absorption spectra and (c) energy level diagram of $CH_3NH_3PbI_3$ (x=0), $CH_3NH_3Pb_{0.85}Sn_{0.15}I_3$ (x=0.15), $CH_3NH_3Pb_{0.7}Sn_{0.3}I_3$ (x=0.3), $CH_3NH_3Pb_{0.5}Sn_{0.5}I_3$ (x=0.5) and $CH_3NH_3SnI_3$ (x=1) perovskite films fabricated on PEDOT:PSS.

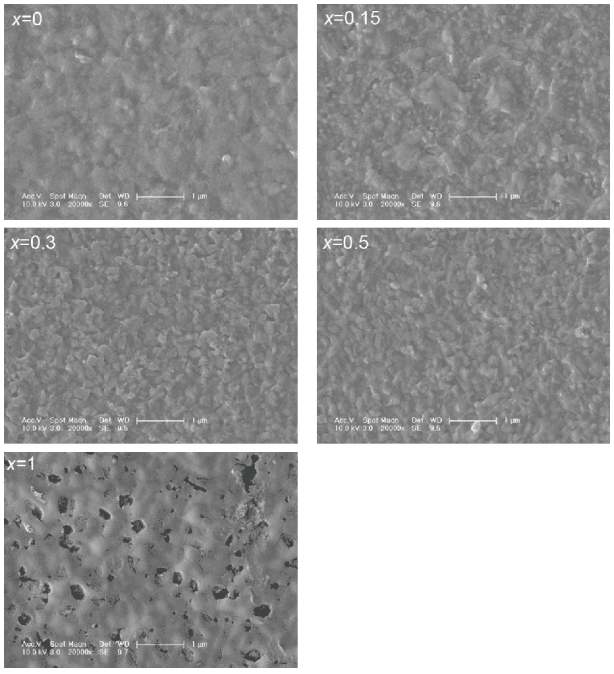

Figure 4 Scanning electron microscopy (SEM) images of $CH_3NH_3PbI_3$, $CH_3NH_3Pb_{0.85}Sn_{0.15}I_3$, $CH_3NH_3Pb_{0.7}Sn_{0.3}I_3$, $CH_3NH_3Pb_{0.5}Sn_{0.5}I_3$ and $CH_3NH_3SnI_3$ perovskite thin films on PEDOT:PSS.

950 nm, the EQE of the photodetector with x=0.3 is greater than 10%, while that with x=0.15 is close to 0. Accordingly, we focus on the photodetectors with x=0 and 0.3 in the following analyses.

The photoresponsivity (R) is the ratio of the photocurrent density (J_{ph}) obtained by a photodetector to the incident light intensity (L_{light}), and can be given as a function of EQE as follows [32,33]: $R=J_{ph}/L_{light}=EQE\cdot q/hv$ (2), where q is the electron charge (1.6×10^{-19} C), h is Planck's constant and v is the frequency of the incident light. As such, R is a good indicator of the efficiency with which photodetectors respond to optical signals. In Fig. 5d, we observe that the two photoresponse curves match well with the EQE spectra of the two photodetectors, with only slight differences in the visible light region. The R for the photodetector with x=0 decreases in the spectral region of 390–800 nm, while the R, with x=0.3, extends up to 1,000 nm. In the visible light region, the maximal R for the photodetectors with x=0 and 0.3 are 0.41 A W^{-1} (at 610 or 780 nm) and 0.39 A W^{-1} (at 680 nm), respectively. In the NIR spectral region of 800–1,000 nm, the R for the photodetector with x=0.3 presents another peak value of 0.35 A W^{-1} (at 890 nm). The R for the photodetectors with x=0.15 and 0.5 are

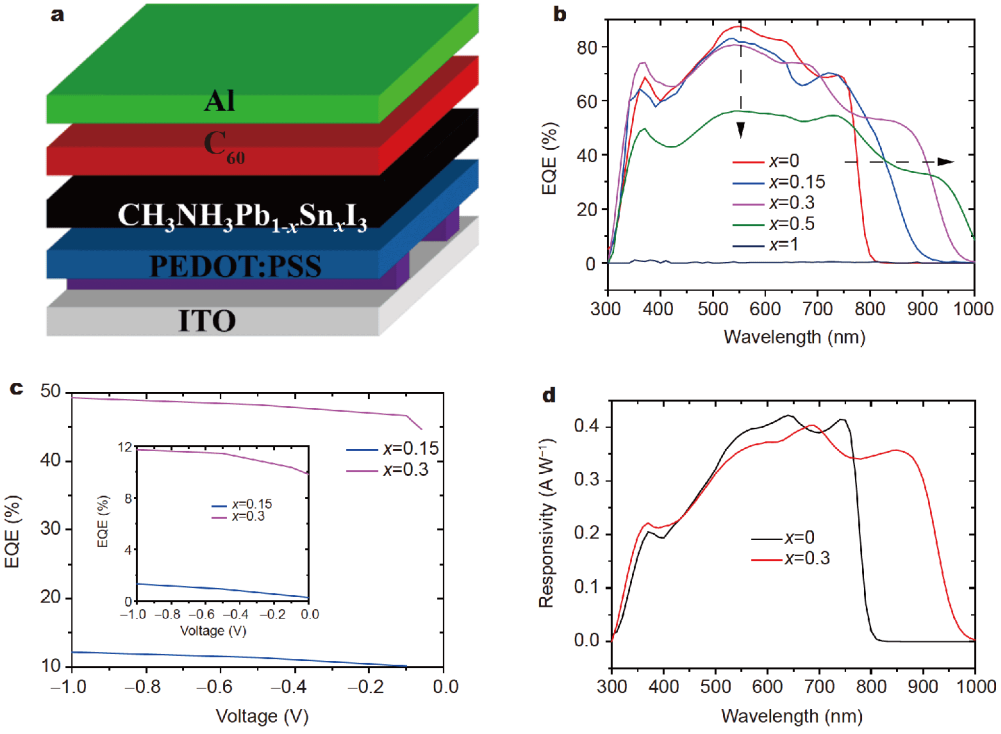

Figure 5 (a) Device structure. (b) Typical EQE spectra obtained under a short circuit condition for all hybrid perovskite photodetectors. (c) EQE spectra of hybrid perovskite photodetectors fabricated with x=0.15 and 0.3 at 900 and 950 nm (in the inset) *vs.* the bias voltage. (d) Photoresponsivity of hybrid perovskite photodetectors with x=0 and 0.3 *vs.* wavelength from 300 to 1,000 nm.

shown in Fig. S1.

Fig. 6a presents the dark current density (J_d) of the photodetectors with x=0 and 0.3 and the results of devices with x=0.15 and 0.5 are also shown in Fig. S2. Here, we find that the two hybrid perovskite photodetectors (x=0 and 0.3) demonstrate a good rectification ratio (±1 V). The J_d for the photodetector with x=0.3 is slightly less than that with x=0.

If, as expected, the short noise comes mainly from J_d [34], $D^*=R/(2qJ_d)^{1/2}$ (3) [35]. Here, we can obtain R and J_d from Figs 5d and 6a, respectively, and plot the calculated values of D^* in Fig. 6b. The maximal D^* obtained for the photodetector with x=0 is 6.5×10^{12} Jones (at 650 or 750 nm) and that with x=0.3 is 7×10^{12} Jones (at 690 nm). In addition, we note that the photodetector with x=0.3 presents another peak of D^* of 6×10^{12} Jones in the NIR region (890 nm), which exhibits a similar trend as that observed for R. In addition, the values of devices with x=0.15 and 0.5 are also shown in Fig. S3.

Generally, the photoresponse time strongly depends on charge transport and collection. As discussed previously [23], the photoresponse time is defined as the time required for the photocurrent output of a photodetector from 10% to 90% of the saturated signal. Similarly, the recovery time is defined as the time required for the photocurrent output of a photodetector from 90% to 10% of the saturated signal. Normalized transient photocurrents in Fig. 7, for the photoresponse and recovery times of the photodetectors with x=0 and 0.3, clearly indicate that the photodetector with x=0 exhibits a shorter response time than that with x=0.3. However, we note that, in an actual application, the pixel size would be smaller and the response time would be expected to be much shorter [14]. The calculated bandwidths of the photodetectors fabricated with x=0 and 0.3 are also shown in Fig. S4. The slower response and greater bandwidth of the device with x=0.3 indicate that, although Sn can broaden the spectral response, it also indeed reduces the speed of charge transport in hybrid perovskite thin films. Moreover, we also observed the attenuation of Sn-based perovskite is faster than Pb-based perovskite, possibly due to the oxide of Sn surface in air. All above results demonstrate Sn is an ideal material to replace Pb to fabricate higher performance perovskite photodetectors. However, further research is required to improve the performance and stability of Sn-based photodetectors in the near future.

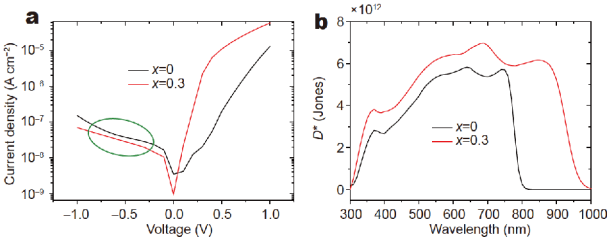

Figure 6 (a) J_d *vs.* voltage and (b) specific detectivity D^* calculated from Equation (3) *vs.* wavelength for the photodetectors fabricated with x=0 and 0.3.

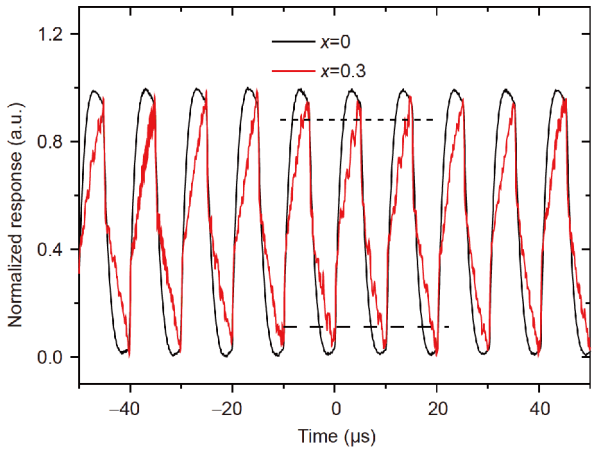

Figure 7 Photoresponse times of the photodetectors fabricated with x=0 and 0.3.

CONCLUSION

We have successfully fabricated high-performance solution-processed $CH_3NH_3Pb_{0.7}Sn_{0.3}I_3$ photodetectors by partially replacing Pb with Sn. The resulting photodetectors exhibit a photoresponse onset up to 1,000 nm, a maximal EQE of approximately 80%, a maximal D^* greater than 7×10^{12} Jones, and a dark current density as small as a few nA cm^{-2}, which are comparable to or better than those obtained for hybrid Pb-based perovskite photodetectors. This indicates that, with further optimization, hybrid Sn-based perovskites may replace hybrid Pb-based perovskites for fabricating high-performance photodetectors with wide spectral response in the future.

Received 15 October 2018; accepted 26 November 2018; published online 7 December 2018

1 Lin Q, Armin A, Nagiri RCR, *et al.* Electro-optics of perovskite solar cells. Nat Photonics, 2015, 9: 106–112
2 Leijtens T, Stranks SD, Eperon GE, *et al.* Electronic properties of meso-superstructured and planar organometal halide perovskite films: charge trapping, photodoping, and carrier mobility. ACS Nano, 2014, 8: 7147–7155
3 Lim KG, Kim HB, Jeong J, *et al.* Boosting the power conversion efficiency of perovskite solar cells using self-organized polymeric

hole extraction layers with high work function. Adv Mater, 2014, 26: 6461–6466
4 Frost JM, Butler KT, Brivio F, *et al.* Atomistic origins of high-performance in hybrid halide perovskite solar cells. Nano Lett, 2014, 14: 2584–2590
5 Xing G, Mathews N, Lim SS, *et al.* Low-temperature solution-processed wavelength-tunable perovskites for lasing. Nat Mater, 2014, 13: 476–480
6 Kojima A, Teshima K, Shirai Y, *et al.* Organometal halide perovskites as visible-light sensitizers for photovoltaic cells. J Am Chem Soc, 2009, 131: 6050–6051
7 Im JH, Lee CR, Lee JW, *et al.* 6.5% Efficient perovskite quantum-dot-sensitized solar cell. Nanoscale, 2011, 3: 4088–4093
8 Kim HS, Lee CR, Im JH, *et al.* Lead iodide perovskite sensitized all-solid-state submicron thin film mesoscopic solar cell with efficiency exceeding 9%. Sci Rep, 2012, 2: 591
9 Jeon NJ, Noh JH, Kim YC, *et al.* Solvent engineering for high-performance inorganic–organic hybrid perovskite solar cells. Nat Mater, 2014, 13: 897–903
10 Zhou H, Chen Q, Li G, *et al.* Interface engineering of highly efficient perovskite solar cells. Science, 2014, 345: 542–546
11 Yang WS, Noh JH, Jeon NJ, *et al.* High-performance photovoltaic perovskite layers fabricated through intramolecular exchange. Science, 2015, 348: 1234–1237
12 Bi D, Tress W, Dar MI, *et al.* Efficient luminescent solar cells based on tailored mixed-cation perovskites. Sci Adv, 2016, 2: e1501170
13 Yang WS, Park BW, Jung EH, *et al.* Iodide management in formamidinium-lead-halide–based perovskite layers for efficient solar cells. Science, 2017, 356: 1376–1379
14 Hao F, Stoumpos CC, Cao DH, *et al.* Lead-free solid-state organic–inorganic halide perovskite solar cells. Nat Photonics, 2014, 8: 489–494
15 Li J, Xu L, Wang T, *et al.* 50-Fold EQE improvement up to 6.27% of solution-processed all-inorganic perovskite $CsPbBr_3$ QLEDs *via* surface ligand density control. Adv Mater, 2017, 29: 1603885
16 Cai B, Li X, Gu Y, *et al.* Quantum confinement effect of two-dimensional all-inorganic halide perovskites. Sci China Mater, 2017, 60: 811–818
17 Zhang X, Yang S, Zhou H, *et al.* Perovskite-erbium silicate nanosheet hybrid waveguide photodetectors at the near-infrared telecommunication band. Adv Mater, 2017, 29: 1604431
18 Dou L, Yang YM, You J, *et al.* Solution-processed hybrid perovskite photodetectors with high detectivity. Nat Commun, 2014, 5: 5404
19 Fang Y, Huang J. Resolving weak light of sub-picowatt per square centimeter by hybrid perovskite photodetectors enabled by noise reduction. Adv Mater, 2015, 27: 2804–2810
20 Lin Q, Armin A, Lyons DM, *et al.* Low noise, IR-blind organohalide perovskite photodiodes for visible light detection and imaging. Adv Mater, 2015, 27: 2060–2064
21 Wang Y, Yang D, Zhou X, *et al.* $CH_3NH_3PbI_3/C_{60}$ heterojunction photodetectors with low dark current and high detectivity. Org Electron, 2017, 42: 203–208
22 Liu Y, Hong Z, Chen Q, *et al.* Integrated perovskite/bulk-heterojunction toward efficient solar cells. Nano Lett, 2015, 15: 662–668
23 Wang Y, Yang D, Zhou X, *et al.* Perovskite/polymer hybrid thin films for high external quantum efficiency photodetectors with wide spectral response from visible to near-infrared wavelengths. Adv Opt Mater, 2017, 5: 1700213
24 Waleed A, Tavakoli MM, Gu L, *et al.* Lead-free perovskite nanowire array photodetectors with drastically improved stability in nanoengineering templates. Nano Lett, 2017, 17: 523–530
25 Li Y, Sun W, Yan W, *et al.* 50% Sn-based planar perovskite solar cell with power conversion efficiency up to 13.6%. Adv Energy Mater, 2016, 6: 1601353
26 Wang Y, Yang D, Zhou X, *et al.* Vapour-assisted multi-functional perovskite thin films for solar cells and photodetectors. J Mater Chem C, 2016, 4: 7415–7419
27 Kieslich G, Sun S, Cheetham AK. Solid-state principles applied to organic–inorganic perovskites: new tricks for an old dog. Chem Sci, 2014, 5: 4712–4715
28 Zhao Y, Zhu K. Organic–inorganic hybrid lead halide perovskites for optoelectronic and electronic applications. Chem Soc Rev, 2016, 45: 655–689
29 Chen Q, Zhou H, Hong Z, *et al.* Planar heterojunction perovskite solar cells *via* vapor-assisted solution process. J Am Chem Soc, 2014, 136: 622–625
30 Liao W, Zhao D, Yu Y, *et al.* Lead-free inverted planar formamidinium tin triiodide perovskite solar cells achieving power conversion efficiencies up to 6.22%. Adv Mater, 2016, 28: 9333–9340
31 Ogomi Y, Morita A, Tsukamoto S, *et al.* $CH_3NH_3Sn_xPb_{(1-x)}I_3$ perovskite solar cells covering up to 1060 nm. J Phys Chem Lett, 2014, 5: 1004–1011
32 Qi J, Han J, Zhou X, *et al.* Optimization of broad-response and high-detectivity polymer photodetectors by bandgap engineering of weak donor–strong acceptor polymers. Macromolecules, 2015, 48: 3941–3948
33 Han J, Qi J, Zheng X, *et al.* Low-bandgap donor–acceptor polymers for photodetectors with photoresponsivity from 300 nm to 1600 nm. J Mater Chem C, 2017, 5: 159–165
34 Gong X, Tong M, Xia Y, *et al.* High-detectivity polymer photodetectors with spectral response from 300 nm to 1450 nm. Science, 2009, 325: 1665–1667
35 Zhou X, Yang D, Ma D. Extremely low dark current, high responsivity, all-polymer photodetectors with spectral response from 300 nm to 1000 nm. Adv Opt Mater, 2015, 3: 1570–1576

Acknowledgements The authors gratefully acknowledge the International Cooperation Foundation of China (2015DFR10700), the National Natural Science Foundation of China (51403203) for the support of this research. Prof. Ma D extends his appreciation to the Distinguished Scientist Fellowship Program (DSFP) at King Saud University, Riyadh, Kingdom of Saudi Arabia for financial support. Prof. Agafonov Vadim thanks the support of the Russian Ministry of Education and Science state assignment (3.3197.2017/ПЧ).

Author contributions Wang Y prepared the figures and wrote the paper. Ma D provided the overall concept and revised manuscript. Yang D, Kim DH, Ahamad T, Alshehri SM and Vadim A classified and analyzed the reference papers. All authors participated in the discussion.

Conflict of interest The authors declare no conflict of interest.

Supplementary information Supporting data are available in the online version of the paper.

Yukun Wang received his BE degree in microelectronics from the College of Electronic Science and Engineering, Jilin University in 2013 and then joined in Prof. Dongge Ma group at Changchun Institute of Applied Chemistry, Chinese Academy of Sciences (CAS), where he obtained his PhD degree in polymer chemistry and physics in 2018. Currently, he is doing his postdoctoral research at Ewha Womans University (South Korea). His research interest includes Pb-based and Pb-free perovskite devices (solar cells and photodetectors).

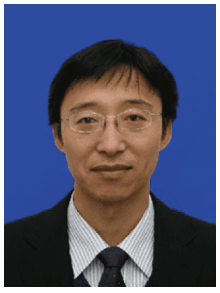

Dongge Ma studied semiconductor device physics at Liaoning University and Jilin University (China), where he received his BSc in 1989 and PhD in 1995, respectively. After additional years as a visiting professor and research fellow in the University Federal do Paranal, Brazil, and Durham University and St. Andrews University, UK, he joined Changchun Institute of Applied Chemistry, CAS, as a professor in 2001. His research interest includes the study of organic optoelectronic devices, including organic light-emitting diodes, organic photovoltaic cells and detectors, metal-based organic transistors, organic lasers, organic/inorganic hybrid perovskite devices and the physics process in these semiconductors.

具有高外量子效率和宽光谱(300~1000 nm)响应的有机-无机杂化锡基钙钛矿光电探测器

王玉坤[1,2], 杨德志[1], 马东阁[1,3*], 金东海[2], Tansir Ahamad[3], Saad M. Alshehri[3], Agafonv Vadim[4]

摘要 有机-无机杂化钙钛矿材料具有载流子迁移率高、扩散长度长、暗电流密度低、吸收边缘锋利等优点, 因而成为用于光电探测的理想材料. 但是, 相对较小的带隙(1.6 eV)限制了这些材料在近红外区的光子捕获效率. 本研究中, 我们利用碘甲胺和铅-锡二元钙钛矿作为探测器的光吸收层, 导电聚合物和富勒烯作为空穴和电子传输层, 铟锡氧化物和铝作为阳极和阴极制备了光电探测器件. 实验结果表明, 当锡的含量达到30%时, 探测器的光谱响应拓宽到1000 nm. 此外, 我们制备的探测器的光谱响应度达到0.39 A W^{-1}, 归一化探测率达到7×10^{12} Jones. 器件的外量子效率在350到900 nm范围内, 均超过50%, 在550 nm处取得最大值, 超过80%.

